Incorporation of rician noise in the analysis of biexponential transverse relaxation in cartilage using a multiple gradient echo sequence at 3 and 7 tesla

Mustapha Bouhrara, David A. Reiter, Hasan Celik, J.-M. Bonny, Vanessa Lukas, Kenneth W. Fishbein, Richard G. Spencer

Incorporation of Rician Noise in the Analysis of Biexponential Transverse Relaxation in Cartilage using a Multiple Gradient Echo Sequence at 3T and 7T

Mustapha Bouhrara[1], **David A. Reiter**[1], **Hasan Celik**[1], **Jean-Marie Bonny**[2], **Vanessa Lukas**[1], **Kenneth W. Fishbein**[1], and **Richard G. Spencer**[1,*]

[1]Laboratory of Clinical Investigation, National Institute on Aging, National Institutes of Health, Baltimore, MD 21224, USA

[2]Imagerie & Transferts, UR370 QuaPA INRA F-63122 Saint Genès Champanelle, France

Abstract

Purpose—Previous work has evaluated the quality of different analytic methods for extracting relaxation times from magnitude imaging data exhibiting Rician noise. However, biexponential analysis of relaxation in tissue, including cartilage, and materials, is of increasing interest. We therefore analyzed biexponential transverse relaxation decay in the presence of Rician noise and assessed the accuracy and precision of several approaches to determining component fractions and apparent transverse relaxation times.

Methods—Comparisons of four different voxel-by-voxel fitting methods were performed using Monte Carlo simulations, and phantom and *ex-vivo* bovine nasal cartilage (BNC) experiments. In each case, preclinical and clinical imaging field strengths of 7T and 3T, respectively, and parameters, were investigated across a range of signal-to-noise ratios (SNR). Results were compared to Cramér-Rao lower bound calculations.

Results—As expected, at high SNR, all methods performed well. At lower SNR, fits explicitly incorporating the analytic form of the Rician noise maintained performance. The much more efficient correction scheme of Gudbjartsson and Patz performed almost as well in many cases. *Ex-vivo* experiments on phantoms and BNC were consistent with simulation results.

Conclusion—Explicit incorporation of Rician noise greatly improves accuracy and precision in the analysis of biexponential transverse decay data.

Keywords

T_2* relaxation; Biexponential mapping; Cartilage; Cramér-Rao lower bound; Accuracy; Precision

[*]Address correspondence to: Richard G. Spencer, M.D., Ph.D., NIH/National Institute on Aging, Intramural Research Program, BRC 04B-116, 251 Bayview Boulevard, Baltimore, MD 21224, Tel: 410-558-8226, spencer@helix.nih.gov.

Introduction

Transverse relaxation time, T_2, obtained through monoexponential analysis of transverse magnetization decay, has been used extensively as a correlate to cartilage status (1). To improve the sensitivity and specificity of such studies, multiexponential analysis of decay has also been undertaken (2-8). Spectroscopic acquisition can detect relatively rapidly relaxing signal components, with T_2 ~0.5-4 ms, generally attributed to collagen-bound water, along with intermediate relaxing components (T_2 ~10-20 ms) likely associated with proteoglycan (PG) and more slowly relaxing components (T_2 ~50-120 ms) attributed to relatively unbound bulk water (6,9). The principal drawback of the spectroscopic approach is the lack of signal localization. To address this, multiexponential analysis has been extended to imaging studies, permitting the creation of component maps (10). This is particularly important for heterogeneous tissues such as articular cartilage, which exhibits depth-dependent structural and compositional variation.

The noise in spectroscopic acquisitions can accurately be modeled as Gaussian. However, the noise distribution in conventional magnitude MR images is Rician. This approaches the Gaussian distribution only for high signal-to-noise ratio (SNR) (11-12), so that the distinction is especially important in settings of limited SNR, including long echo-time images (13). Substantial improvements in T_1, T_2 and diffusion mapping have been reported when the proper noise model is used, to an extent that depends upon which of several analysis methods is implemented (13-18). However, a systematic analysis examining improvements using Rician noise modeling in the more complicated case of multiexponential relaxation has not been undertaken. Thus, our principle aim is to evaluate the performance of different methods for incorporating Rician noise into the analysis of multiexponential decay; we have restricted our analysis to the biexponential case.

The use of a spin-echo imaging sequence results in minimum echo times, TE_{min}, of several milliseconds (19-20), rendering quantification of rapidly relaxing signal components problematic. Alternatively, much shorter echo times may be achieved using a gradient echo sequence thereby observing T_2^* rather than T_2 decay. The relatively rapid T_2^* signal loss limits the duration of the relaxation signal available for sampling, but this is compensated by shorter echo times and decreased echo spacing. Attempts to describe multicomponent T_2^* decay in cartilage have recently been undertaken (21-22). Work on human cadaveric patellae (23) using an ultrashort echo time (UTE) MRI-sequence with $TE_{min} = 8\ \mu s$, suggests that the short T_2^* water fraction may serve as a biomarker of cartilage degeneration. Further analyses of several human connective tissues using UTE imaging has also been reported (24-25). Assuming biexponential decay, a short T_2^* component, ~0.5-3 ms, has been identified and attributed to water molecules trapped within collagen and PG. A long T_2^* component, ~20-30 ms, was attributed to bulk water.

The UTE sequence used in these two-component relaxation studies requires specialized hardware and software. Relaxation time components in the range of $T_2^* \sim 13\ ms$ can also be detected with a conventional multi-gradient echo (MGE) sequence (TE_{min} ~1-2 ms). Therefore, our secondary goal is to investigate the use of the MGE sequence to map

biexponential T_2^* components in cartilage. We use bovine nasal cartilage (BNC) as a model cartilage system; BNC exhibits macromolecular structure and composition comparable to that of articular cartilage, but without the complexity of its layered structure.

A two-component relaxation model represents a reasonable implementation of multi-component analysis in cartilage given what is known from previous literature. Further, although much more informative than conventional monoexponential analysis, biexponential analysis required only modest SNR and so may be relatively practical for clinical applications.

We first review the theory of Rician noise. We then apply Cramér-Rao lower bound (CRLB) theory to establish a standard for comparison for our estimates of compartment fractions and transverse relaxation times. Next, we describe four different voxel-by-voxel fitting methods and related Monte Carlo (MC) simulations to evaluate the accuracy and precision of derived parameters. After extensive simulation results, we present data obtained from a two-component phantom and from cartilage explants, using both the pre-clinical field strength of 7T and the clinical field strength of 3T.

Theory

Signal distribution function

Given Gaussian-distributed noise of equal variance in the real and imaginary channels of complex-valued MRI data, the probability distribution of magnitude image data is given by the Rician probability density function (PDF) (11):

$$P_{Rice}\left(S_M|A(TE,\boldsymbol{\theta}),\sigma\right)=\frac{S_M}{\sigma^2}e^{\left(\frac{-\left(A^2(TE,\boldsymbol{\theta})+S_M{}^2\right)}{2\sigma^2}\right)}\,I_0\left(\frac{A(TE,\boldsymbol{\theta})S_M}{\sigma^2}\right) \quad [1]$$

where $A(TE, \theta)$ is the magnitude of the underlying noise-free signal as a function of parameters θ and TE, S_M is the amplitude of the measured magnitude signal, I_0 is the modified zero-order Bessel function of the first kind, and σ^2 is the variance of the noise in each of the two channels. The expectation value of S_M is given by (14-15, 26-27)

$$\begin{aligned}E_{Rice}\left[A(TE,\boldsymbol{\theta}),\sigma\right]&=\int_0^\infty S_M\,P_{Rice}(S_M|A(TE,\boldsymbol{\theta}),\sigma)\,dS_M\\&=\sigma\sqrt{\tfrac{\pi}{2}}e^{-\alpha}\left((1+2\alpha)\,I_0(\alpha)+2\alpha\,I_1(\alpha)\right)\end{aligned} \quad [2]$$

where $\alpha = (A(TE, \theta)/2\sigma)^2$ and I_1 is the modified first-order Bessel function of the first kind. For $A(TE, \theta) \gg \sigma$, the PDF of the Rician distribution approximates a Gaussian distribution, P_{Gauss}, with mean value $A(TE, \theta)$ and standard deviation σ (12, 16)

$$P_{Gauss}\left(S_M|A\left(TE,\boldsymbol{\theta}\right),\sigma\right)=\frac{1}{\sigma\sqrt{2\pi}}e^{\left(\frac{-\left(S_M-A(TE,\boldsymbol{\theta})\right)^2}{2\sigma^2}\right)} \quad [3]$$

See Fig. 1a. The expectation value of S_M for the Gaussian distribution is

$$E_{Gauss}[S_M] = \int_{-\infty}^{+\infty} S_M \, P_{Gauss}(S_M | A(TE, \boldsymbol{\theta}), \sigma) \, dS_M = A(TE, \boldsymbol{\theta}) \quad [4]$$

Noise estimation

In a background region of an image, $A(TE, \theta) = 0$ so that Eq. 1 reduces to the Rayleigh distribution (12, 28-29):

$$P_{Rayleigh}(S_M | \sigma) = \frac{S_M}{\sigma^2} e^{-\left(\frac{S_M^2}{2\sigma^2}\right)} \quad [5]$$

From this, the expectation value of the magnitude noise is (16)

$$E_{Rayleigh}[S_M] = \int_0^{\infty} S_M \, P_{Rayleigh}(S_M | \sigma) \, dS_M = \sigma \sqrt{\frac{\pi}{2}} \quad [6]$$

Eq. 6 permits accurate estimation of noise by measurement of average signal intensity within a background region of interest (30).

Cramér-Rao lower bound

The CRLB provides an explicit theoretical limit to the precision with which a parameter can be determined using an unbiased estimator (31-36). Calculation of the CRLB requires inversion of the Fisher matrix, **F**, (37). For data obtained at time points t_n and fit to a parameterized curve $A_n(TE, \theta)$, defined by a vector θ of M parameters, and with the assumption of equal standard deviations σ at each data point, the elements of the Fisher matrix for the Rician distribution, Eq. 1, are given by (14, 38)

$$F_{ij,Rician}(\boldsymbol{\theta}; TE, \sigma) = \frac{1}{\sigma^2} \left(\sum_{n=1}^{N} \frac{\partial A_n(TE, \boldsymbol{\theta})}{\partial \theta_i} \frac{\partial A_n(TE, \boldsymbol{\theta})}{\partial \theta_j} \right) R(A_n(TE, \boldsymbol{\theta}), \sigma) \quad [7]$$

where

$$R(A_n(TE, \boldsymbol{\theta}), \sigma) = -\frac{A_n^2(TE, \boldsymbol{\theta})}{\sigma^2} + \int_0^{\infty} \frac{y^3}{\sigma^2} e^{\frac{-\left(y^2 + A_n^2(TE, \boldsymbol{\theta})\right)}{2\sigma^2}} \frac{I_1^2\left(\frac{yA_n(TE, \boldsymbol{\theta})}{\sigma^2}\right)}{I_0\left(\frac{yA_n(TE, \boldsymbol{\theta})}{\sigma^2}\right)} dy \quad [8]$$

Because the integral in Eq. 8 cannot be solved analytically, R can be calculated by numerical integration for different values of $A_n(TE, \theta)/\sigma$ (38). For $A(TE, \theta) \gg \sigma$, the value of R approaches 1 (Fig.1b), in which case the Fisher matrix for the Rician distribution becomes identical to that of the Gaussian distribution:

$$F_{ij,Gaussian}(\boldsymbol{\theta}; TE, \sigma) = \frac{1}{\sigma^2} \left(\sum_{n=1}^{N} \frac{\partial A_n(TE, \boldsymbol{\theta})}{\partial \theta_i} \frac{\partial A_n(TE, \boldsymbol{\theta})}{\partial \theta_j} \right) \quad [9]$$

We can now define a vector $\mathbf{CRLB}=\sqrt{diag(\mathbf{F}^{-1}(\boldsymbol{\theta};TE,\sigma))}$. Then the maximum precision of an unbiased parameter estimate $\hat{\theta_i}$ of the parameter θ_i is given by

$$CRLB(\hat{\theta}_i)=\sqrt{F_{ii}^{-1}(\boldsymbol{\theta};TE,\sigma)} \quad [10]$$

Methods

Methods comparison

We consider a model $A(TE, \theta)$ describing biexponential relaxation as a function of echo time, *TE*, and parameter set $\boldsymbol{\theta}=(\ PD \quad F_s \quad T_{2,s}^* \quad T_{2,l}^*\ )$

$$A(TE,\boldsymbol{\theta})=PD\left(F_s\,exp\left(-TE\Big/T_{2,s}^*\right)+(1-F_s)exp\left(-TE\Big/T_{2,l}^*\right)\right) \quad [11]$$

where proton density, *PD*, represents signal amplitude at *TE* = 0 and incorporates T_1 weighting, proton density, coil sensitivity and other machine factors. F_s is the fraction of the short T_2^* component and $T_{2,s}^*$ and $T_{2,l}^*$ are short and long apparent spin-spin relaxation times, respectively.

To obtain a robust method for voxel-by-voxel estimation of all parameters of the vector θ, four different methods were compared, using both simulations and phantom measurements, as a function of SNR. The first method, M_R, makes full use of the expectation value of the Rician distribution given by Eq. 2 and involves nonlinear least-squares (NLLS) minimization of $S_M - E_{Rice}[A(TE, \theta), \sigma]$. The second, traditional approach, M_T, uses the Gaussian estimator in Eq. 4, and consists of NLLS minimization of $S_M - E_{Gauss}[S_M]$, that is, $S_M - A(TE, \theta)$, where $A(TE, \theta)$ is given by Eq. 11. The third method, M_{Mc}, based on the McGibney correction scheme (18, 39), consists of NLLS minimization of $S_M^2 - E_{Gauss}[S_M^2]$, where $E_{Gauss}[S_M^2]=A^2(TE,\boldsymbol{\theta})+2\sigma^2$. The last method, M_G, based on the Gudbjartsson correction scheme (16), consists of the NLLS minimization of $\sqrt{|S_M^2-\sigma^2|}-E_{Gauss}[S_M]$. Note that in all cases, *PD* was fit along with the other parameters.

The standard deviation of the noise, σ, was determined using Eq. 6 from the mean signal of background regions of all images acquired at each *TE*, after manual segmentation. This eliminates one degree of freedom in the NLLS analysis. Analytic first derivatives of $E_{Rice}[S_M]$, $E_{Gauss}[S_M^2]$ and $E_{Gauss}[S_M]$ with respect to each parameter of the vector θ (see Appendix) were used in the minimization for fast and robust convergence. In the phantom and *ex-vivo* studies, initial voxel-wise estimates of $\hat{T}_{2,l,init}^*$ and $\hat{PD}_{l,init}$ were calculated from an NLLS fit of the entire echo train to a monoexponential decay function. Modified data, $S_{M,s}$, representing an estimate of the signal attributed to the short relaxation time component, were created according to

$$S_{M,s}(TE)=\hat{PD}_{s,init}\,exp\left(-TE\Big/\hat{T}^{*}_{2,s,init}\right)=S_{M}(TE)-\left(\hat{PD}_{l,init}\,exp\left(-TE\Big/\hat{T}^{*}_{2,l,init}\right)\right) \quad [12]$$

Initial estimates $\hat{T}_{2,s,init}$ and $\hat{PD}_{s,init}$ were likewise obtained from an NLLS fit of $S_{M,s}$ to a monoexponential decay. Finally, initial estimates for $\hat{PD}_{init}$ and $\hat{F}_{s,init}$ were given by $\hat{PD}_{init}=\hat{PD}_{s,init}+\hat{PD}_{l,init}$ and $\hat{F}_{s,init}=\hat{PD}_{s,init}/\hat{PD}_{init}$, respectively. This procedure ensured relatively accurate initial parameter estimates and therefore rapid convergence of the NLLS algorithm. All NLLS fits were performed with the Levenberg-Marquardt algorithm (40-41) using Matlab (MathWorks, Natick, MA, USA).

Monte Carlo simulations

Simulations were performed using computer generated images (70 × 70 = 4900 voxels) exhibiting biexponential relaxation according to Eq. 11. Input simulation parameters were chosen to reflect either pre-clinical imaging conditions (PCI) at 7T, or clinical imaging conditions (CI) at 3T. These parameter choices closely matched values obtained from studies performed on our phantoms (*see Phantom study section*) which were constructed to exhibit T_2^* values close to those reported for cartilage in the literature (21-25).

PCI simulations consisted of a shorter component with $T^*_{2,s}=3.6\ ms$ and fraction F_s = 0.5, and a longer component with $T^*_{2,l}=41\ ms$ and $F_l = 1 - F_s = 0.5$. A total of 32 images were generated with TE_n increasing uniformly from 0.97 to 54.6 ms in increments of 1.73 ms. CI simulations consisted of a shorter component with $T^*_{2,s}=3.3\ ms$ and fraction F_s = 0.5, and a longer component with $T^*_{2,l}=38.1\ ms$ and F_l = 0.5. A total of 32 images were generated with TE_n increasing uniformly from 2.6 to 77 ms in increments of 2.4 ms. Additional simulations for different choices of fractions and relaxation times, as shown in table 2, were performed to further illustrate our results and to investigate the effect of F_s and the ratio $T^*_{2,l}/T^*_{2,s}$ on both the accuracy and precision of parameters estimation.

For all simulations, Rician noise was added to produce images with SNR ranging from 15 to 100 in increments of 5. Specifically, the noisy images, S_M, at each *TE* were obtained by adding Gaussian noise in both the real, $I_r(TE) = A(TE, \theta) + N_r$, and the imaginary, $I_i(TE) = N_i$, parts of the complex images, where N_r and N_i were random numbers generated from a Gaussian distribution with zero mean, and with standard deviation σ. Magnitude images, S_M, were then created using the following expression

$$S_M(TE)=\sqrt{I_r{}^2(TE)+I_i{}^2(TE)} \quad [13]$$

PD was kept constant and σ was varied to obtain the desired SNR.

MRI hardware and MGE sequence description

Experiments were performed on both a 7T small animal MRI scanner (Bruker Biospin GmbH, Rheinstetten, Germany) using a linearly polarized birdcage coil and a 3T MRI whole body system (Achieva, Philips Medical Systems) equipped with a quadrature transmit/receive head coil. T_2^*-weighted images were acquired using 3D MGE sequences. Only images with the same polarity of read-out gradient direction were acquired to prevent alternation in the direction of chemical shift artifacts and to avoid image misregistration due to the static magnetic field gradients (43-44). To correct geometric distortion introduced by spatial variations of the magnetic field B_0 (45), MGE images were registered (46-47).

Phantom study

Two similar rectangular tubes (8 × 4 cm) filled with deionized water were doped with different concentrations of $CuSO_4$. The resulting T_2^* values as given below were obtained by acquiring high SNR images from each tube independently and fitting them to a monoexponential function (13). The tubes were then placed together in the MRI system and images were acquired through the center of each tube. Complex images were added together with consistent phases to obtain a composite image representing a biexponential phantom. The resulting magnitude images were fitted according to the biexponential models described above. To be more explicit, T_2^*-weighted images were obtained from each tube as described above. The phase shift between each voxel of the image from the first tube and each voxel of the image from the second tube was calculated from the complex data. A phase correction was then applied to complex data from the second image so that the two images had the same phase. This procedure accurately produced a two-component dataset, while minimizing artifacts associated with the susceptibility difference between the tube walls and each solution.

For PCI conditions at 7T, the first and second compartments respectively exhibited parameters F_s = 50%, $T_{2,s}^*$=$3.6 \pm 0.3 ms$, F_l = 50% and $T_{2,l}^*$=$41 \pm 4.4 ms$. Biexponential analysis was performed on data consisting of 32 T_2^*-weighted images with TE_n increasing linearly from 0.97 to 54.6 ms in steps of 1.73 ms. Other image parameters included TR = 200 ms, field of view (FOV) = 50 × 50 × 16 mm^3, matrix = 100 × 100 × 16 and spectral bandwidth (SBW) = 200 kHz. The acquisition time for one signal average was ~5 min.

For CI at 3T, the first compartment exhibited F_s = 50% and $T_{2,s}^*$=$3.3 \pm 0.36 ms$ while the second one had F_l = 50% and $T_{2,l}^*$=$38.1+3.5 ms$. 32 T_2^*-weighted images were acquired with TE_n increasing linearly from 2.6 to 77 ms in steps of 2.4 ms. Other image parameters included TR = 200 ms, FOV = 80 × 80 × 15 mm^3, matrix = 88 × 176 × 15 and SBW = 96 kHz. The acquisition time for one signal average was ~9 min. Linear combinations of the data from the two phantoms were created to obtain Rician-distributed magnitude image datasets with different compartment fractions. The results of the biexponential fits of these datasets are shown in Table 3 and illustrate the effect of F_s on the accuracy and precision of parameter estimation with more disparate compartment sizes.

For both PCI and CI, the number of signal averages was varied from 1 to 32 to produce images with different SNR.

Ex-vivo study

The central part of the nasal septum cartilage of a young cow (Green Village Packing, Green Village, NJ) was removed and moistened with Dulbecco's phosphate buffered saline (DPBS) and stored at 4 °C until imaged. During scanning, the sample was immersed in Fluorinert FC-77 (Sigma-Aldrich, St. Louis, MO) to maintain sample hydration and to avoid artifacts due to susceptibility differences between the sample and surrounding air. All imaging was performed at room temperature.

PCI *ex-vivo* image acquisitions consisted of three scans of 32 T_2^*-weighted images with different first echo times, TE_1 = 0.86 ms, 1.6 ms and 2.6 ms; these datasets were interleaved to ensure adequate sampling of the signal decay, particularly for the fast-relaxing component. Other image parameters included ΔTE = 3.1 ms, TR = 400 ms, FOV = 70 × 50 × 15 mm^3, SBW = 152 kHz and matrix = 140 × 100 × 20, resulting in a voxel size of 0.5 × 0.5 × 0.75 mm^3. The acquisition time for one signal average per scan was ~10 min.

CI *ex-vivo* image acquisitions consisted of two scans of 32 T_2^*-weighted images with different first echo times, TE_1 = 2 ms and 3 ms, which were again interleaved. Other imaging parameters included ΔTE = 2.4 ms, TR = 1000 ms, FOV = 40 × 75 × 8 mm^3, matrix = 77 × 167 × 10, voxel size = 0.52 × 0.45 × 0.8 mm^3 and SBW = 99 kHz. The acquisition time for one signal average per scan was ~28 min.

For both PCI and CI, the number of signal averages was varied from 1 to 16 to produce images with different SNR.

Bias, dispersion and mean-squared-error calculations

The performance of each method was evaluated by calculating the relative bias, dispersion, and mean-squared-error in each fitted parameter. The relative bias, a measure of accuracy, was defined as the difference between the true value, θ_i, and the mean of the estimated value over multiple noise realizations, $\hat{\theta}_i$, normalized by the true value, given by $100 * |\theta_i - \bar{\hat{\theta}}_i|/\theta_i$. In simulations, the true values were known but in the phantom study they were obtained from a monoexponential fit of high SNR data acquired from each phantom compartment separately. The values obtained were used in the MC simulations described above. The relative dispersion was defined as the relative standard deviation, 100 * SD($\hat{\theta}_i$)/θ_i, and was compared to the minimal relative dispersion given by 100 * $CRLB_i/\theta_i$. The mean-squared-error (MSE) a measure including both precision and accuracy was defined as the sum of the square of the bias of the estimator and its variance by the expression $|\theta_i - \bar{\hat{\theta}}_i|^2 + \mathrm{SD}^2(\hat{\theta}_i)$ (30).

Relative bias, relative dispersion and MSE were calculated as a function of SNR for F_S, $T_{2,s}^*$ and $T_{2,l}^*$. SNR was defined as $\sqrt{\bar{S}(\mathrm{TE}_1)^2 - 2\sigma^2}/\sigma$ (18), where TE_1 is the shortest echo time at which data were acquired. In simulations, $S(TE_1)$ was known but in phantom and *ex-vivo*

studies it was calculated as the mean signal from a large region covering almost the entire sample.

Voxels with extreme outliers (VEO) were removed for each method using Tukey's method (42). A VEO was defined as a voxel whose value was less than $Q_1(\hat{\theta_i}) - 3Q_I(\hat{\theta_i})$ or greater than $Q_3(\hat{\theta_i}) + 3Q_I(\hat{\theta_i})$, where $Q_1(\hat{\theta_i})$, $Q_3(\hat{\theta_i})$ and $Q_I(\hat{\theta_i})$ represent the first quartile, the third quartile and the interquartile interval of estimated parameter, $\hat{\theta_i}$, respectively.

In contrast to the simulations and the phantom studies, the true parameter values (*i.e.* F_s, $T^*_{2,s}$ and $T^*_{2,l}$) for the BNC sample were unknown. Therefore, the bias and dispersion cannot be directly evaluated. Instead, we assessed the accuracy and precision of each fitting method for the estimation of F_s, $T^*_{2,s}$ and $T^*_{2,l}$ as a function of SNR by considering the maps obtained at high SNR using M_R as the reference maps. Note that the maps obtained at high SNR with all four methods were similar. For each estimated parameter, the maps obtained at lower SNRs were compared to the reference maps. Because of the heterogeneities of the parametric maps, absolute instead of relative bias and dispersion were considered. The absolute bias was defined using the difference between the mean estimated value, $\overline{\hat{\theta}}_i$, over voxels exhibiting biexponential behavior in the parametric map and its equivalent in the reference map, $\overline{\hat{\theta}}_{i,ref}$, through $|\overline{\hat{\theta}}_{i,ref} - \overline{\hat{\theta}}_i|$. The absolute dispersion is a measure of the standard deviation and was defined as $\sqrt{(1/M)\sum_{j=1}^{M}\left(\hat{\theta}_i^j - \hat{\theta}_{i,ref}^j\right)^2}$, where M is the number of voxels exhibiting biexponential behavior. These voxels were defined as those for which $AIC_{c,mono}/AIC_{c,bi} \geq 1$ and $0 < F_s < 0.2$, where $AIC_{c,mono}$ and $AIC_{c,bi}$ are corrected Akaike Information Criteria (48) obtained from high SNR data using the M_R method and assuming monoexponential and biexponential fit functions, respectively. The AIC_c in our case is given by

$$AIC_c = 2P + \frac{2P\,(P+1)}{N-P-1} + N\,log\left(\frac{RSS}{N}\right) \quad [14]$$

where N is the number of measurements defining the experimental curve, P is the number of fitted parameters and RSS is the residual sum of squares of the fit. Note that the additional criterion of $0 < F_s < 0.2$ was used to avoid attributing biexponential character to voxels displaying nonexponential decay that were numerically well-fit to biexponentials, but that provided clearly aberrant values of F_s. This latter criterion was based on our previous spectroscopic work establishing approximate bounds on F_s.

Measures of goodness-of-fit summarize the discrepancy between a measured quantity Q, and the expected value $E[Q]$, of a given model. The most commonly used goodness of fit test is the chi-square, χ^2, given by

$$\chi^2 \propto \sum_{n=1}^{N} \frac{(Q - E[Q])^2}{E[Q]} \quad [15]$$

where $Q = S_M$ for M_G, M_R and M_T and $Q=S_M^2$ for M_{Mc}. At each SNR level, χ^2 was calculated voxel-by-voxel using each of the four investigated methods. The goodness-of-fit of each method was then evaluated using the mean chi-square, $\overline{\chi^2}$, over voxels exhibiting biexponential behavior.

Results

Monte Carlo simulations

Table 1 shows the mean and the maximum of the number of VEO removed for each of the four methods evaluated over the range 15 ≤ SNR ≤ 40. Values are given in percent relative to the total number of 4900 voxels. The mean number of VEO was almost identical for all four methods. At low SNR, the number of VEO removed was slightly lower with M_G, and M_R as compared to the traditional M_T and M_{Mc}, methods, representing a modest improvement in performance. Also, the mean and the maximum number of VEO in the PCI analysis were smaller than in the CI analysis. For SNR > 40, the mean number of VEO was less than 1% in all cases.

Figs. 2 shows the relative bias, relative dispersion and MSE for the estimates of F_s, $T_{2,s}^*$ and $T_{2,l}^*$ as a function of SNR for PCI (Fig. 2a) and CI (Fig. 2b). For SNR > 30 in PCI and SNR > 40 in CI, all four methods showed a small bias (< 2%) in the estimation of each of the three parameters (first row of Figs. 2a-2b). However, the bias increased rapidly with decreasing SNR, particularly for M_T. The M_{Mc} showed somewhat smaller bias compared to M_T. Although the bias remained substantial at low SNR, both M_R and M_G allowed considerable reduction of this bias compared to M_{Mc} and M_T. The relative accuracies of M_R and M_G were very similar for each estimated parameter and for both PCI and CI over the entire range of SNR.

The second rows of Figs 2a and 2b show that the relative dispersion obtained with M_G and M_R was comparable to the dispersion given by CRLB, representing an optimum, for PCI and CI over the entire range of SNR. The relative precision obtained with M_T and M_{Mc} in the estimation of F_s and $T_{2,s}^*$ was comparable with the CRLB only for SNR > 40, and estimation of $T_{2,l}^*$ only for SNR > 60. To attain relative dispersion less than 10%, PCI required SNR > 25 for F_s and $T_{2,l}^*$ for M_T, M_G or M_R. Using M_{Mc}, SNR > 30 and SNR > 45 were needed for F_s and $T_{2,l}^*$ respectively. For $T_{2,s}^*$, SNR > 60 was necessary using M_T, M_G or M_R and SNR > 75 for M_{Mc}. To achieve relative dispersion less than 10% in CI, SNR > 35 was necessary for F_s using any of the four methods. For $T_{2,l}^*$ and $T_{2,s}^*$, SNR > 20 and SNR > 80 were needed using M_T, M_G or M_R, and SNR > 30 and SNR > 105 using M_{Mc}, respectively.

The MSE for all investigated methods was almost identical for all fitting methods for SNR > 50 (third rows of Figs. 2a and 2b). However, for low and moderate SNR, M_T and M_{Mc} resulted in a greater MSE as compared to M_G and M_R. M_G and M_R showed virtually identical MSE over the entire range of SNR for each estimated parameter for both PCI and CI.

We investigated five other representative combinations of F_s, $T^*_{2,s}$ and $T^*_{2,l}$ using in all cases SNR = 15 and 100, TE_1 = 2 ms, ΔTE = 2 ms and 32 echoes. Table 2 shows the relative accuracy and precision obtained in the estimation of F_s, $T^*_{2,s}$ and $T^*_{2,l}$ using the four methods investigated. In general, both bias and dispersion were found to increase with a decreasing ratio $T^*_{2,l}/T^*_{2,s}$. In addition, bias and dispersion increase with a greater disparity between component sizes.

For SNR = 35, the parameter mean computation times using a 4 GHz desktop computer over several noise realizations for M_T, M_{Mc}, M_G and M_R were ~15 ms, ~19 ms, ~15 ms and ~170 ms, respectively.

Phantom study

Fig. 3 shows representative F_s, $T^*_{2,s}$ and $T^*_{2,l}$ maps obtained using M_T, M_{Mc}, M_G and M_R from phantom measurements obtained at 7T and 3T. For SNR > 90, all four methods yielded virtually indistinguishable maps. However, for low SNR, the parametric maps were substantially more heterogeneous using M_T and M_{Mc} compared to M_G and M_R. Figs 4 shows there relative bias, relative dispersion and MSE determined from the phantom measurements of F_s, $T^*_{2,s}$ and $T^*_{2,l}$ as a function of SNR for PCI (Fig. 4a) and CI (Fig. 4b), respectively. The relative bias, relative dispersion and MSE were substantially lower for M_G and M_R as compared to M_T and M_{Mc}, especially for low SNR. For moderate-to-high SNR, all methods were similar. Unlike M_T and M_{Mc}, the relative dispersion of M_G and M_R was close to the CRLB limit for all estimated parameters. Note that the curves in Figs 4 were obtained after VEO removal.

We investigated the effect of F_s for three values of SNR, and CI experimental parameters. Datasets were created as described in Methods. Table 3 shows the relative accuracy and precision obtained in the estimation of F_s, $T^*_{2,s}$ and $T^*_{2,l}$ using the four methods. In general, both bias and dispersion increased with a greater disparity between component sizes.

Ex-vivo study

Fig 5 shows representative T^*_2-weighted images of BNC obtained at 7T and 3T, and corresponding parametric maps of F_s, $T^*_{2,s}$ and $T^*_{2,l}$ obtained at high SNR using M_R. The T^*_2-weighted images show susceptibility-induced rapid signal decay in the vicinity of blood vessels. Biexponential decay was seen in ~20% and ~26% of voxels at PCI and CI respectively, with the others displaying monoexponential decay, or, in the case of voxels near vessels, nonexponential decay. Our quantitative results were based on analysis of the voxels exhibiting biexponential decay. In those samples, short fractions of ~0.08 and ~0.07 under PCI and CI conditions, respectively, were observed. $T^*_{2,s}$ and $T^*_{2,l}$ were very heterogeneous exhibiting mean values of about ~3.9 ms and ~60 ms, respectively, for PCI and ~4.6 ms and ~67 ms for CI.

Fig 6 shows the $\overline{\chi^2}$ calculated over voxels exhibiting biexponential behavior for each level of SNR and for each investigated method; these voxels were identified in parametric maps

obtained at high SNR using the M_R. As expected, $\overline{\chi^2}$ decreases rapidly with increasing SNR. At low SNR, M_R is clearly superior to the other methods of analysis, while at moderate and high SNR, all methods produced similar values of $\overline{\chi^2}$. These results validate our use of the parametric maps obtained at high SNR with M_R as reference maps for calculating the accuracy and precision of F_s, $T^*_{2,s}$ and $T^*_{2,l}$ for BNC.

Figs 7 presents the absolute bias and dispersion of the estimates for the three parameters for BNC as a function of SNR at 7T (Fig. 7a) and 3T (Fig. 7b). The curves indicate monotonic, roughly linear trend in bias and dispersion for all estimated parameters as a function of SNR. All methods performed similarly at high SNR, while M_R was superior for low-to-moderate SNR.

Discussion

Fitting methods

The analyses of Karlsen *et al*. (14) and Raya *et al*. (13) evaluate estimates of T_1 and T_2 from monoexponential data with explicit incorporation of the underlying Rician noise distribution. In this conventional formulation, only a single relaxation time, and no component fraction, is available from the data. Our treatment extends this work to the biexponential case and considers the accuracy and precision with which the component fraction ratio and the two relaxation times can be estimated. Our data set was generated using a MGE sequence, so that the relaxation times under consideration were T_2^* rather than T_2; the underlying analysis is of course generalizable to any biexponential data curve.

Our analysis includes three of the methods examined by Raya *et al*. These methods were denoted EXP, SQEXP and NCEXP in that work, and correspond to M_T, M_{Mc} and M_R in our study, respectively. Raya *et al*. found NCEXP, which explicitly incorporates the correct noise model, to yield the most reliable results. The reduced accuracy of the other methods was most notable in the low-to-modest SNR regime. Improvements were observed with SQEXP compared to EXP. Our results for the biexponential model were on the whole consistent with these results. Most notably, M_R produced the best parameter estimates, in spite of the more complex analytic expectation value of the Rician distribution, Eq. 2, for the biexponential model. In particular, the expression for the noise-free signal, $A(TE, \theta)$, contains 4 free parameters, Eq. 11, rather than the 2 free parameters required for the monoexponential model. We found that in spite of this additional model complexity, the performance of the NLLS minimization was not degraded for M_R.

Simulation (Fig. 2) and phantom (Fig. 4) studies indicated that M_G performed almost as well as M_R over a large range of SNR. This is consistent with the results of Karlsen *et al*. (14) in their study of monoexponential decay showing that the absolute bias of the M_G method was comparable with the absolute bias of the M_R method. In addition, the analysis of Gudbjartsson and Patz (16) indicates that their correction to image amplitude yields a PDF for the corrected image, $\tilde{A}=\sqrt{|S_M^2-\sigma^2|}$, given by, for SNR ≥ σ,

$$P(\tilde{A}|A(TE,\boldsymbol{\theta}),\sigma)=\tilde{A}P_{Rice}\left(\sqrt{\tilde{A}^2+\sigma^2}|A(TE,\boldsymbol{\theta}),\sigma\right)/\sqrt{\tilde{A}^2+\sigma^2},$$

and for SNR < σ,

$$P(\tilde{A}|A(TE,\boldsymbol{\theta}),\sigma) = \tilde{A}\left(\left(P_{Rice}\left(\sqrt{\tilde{A}^2+\sigma^2}|A(TE,\boldsymbol{\theta}),\sigma\right)/\sqrt{\tilde{A}^2+\sigma^2}\right) + \left(P_{Rice}\left(\sqrt{\sigma^2-\tilde{A}^2}|A(TE,\boldsymbol{\theta}),\sigma\right)/\sqrt{\sigma^2-\tilde{A}^2}\right)\right),$$ which approximates the Rician PDF. This comparability of performance between M_R and M_G may also result partially from the decreased complexity of these expressions as compared to the full biexponential signal model incorporating Rician noise, as noted above.

M_{Mc}, showed relatively large dispersion and minimal bias improvement over M_T. This is also consistent with the monoexponential analyses of Karlsen *et al*. (14) and the probability distribution analyses of Gudbjartsson and Patz (16) who attribute this to the fact that the distribution of the noise for the corrected power images, $\tilde{A}^2=S_M^2-2\sigma^2$, given by $P(\tilde{A}^2|A(TE,\boldsymbol{\theta}),\sigma)=(1/2\sigma^2)\,exp\left(-\left(\tilde{A}^2+2\sigma^2+A^2(TE,\boldsymbol{\theta})\right)/2\sigma^2\right)\,I_0\left(A(TE,\boldsymbol{\theta})\sqrt{\tilde{A}^2+2\sigma^2}/\sigma^2\right)$ approximates neither the Rician nor the Gaussian distribution at low SNR. To improve the precision of M_{Mc}, Raya *et al*. (13) suggested use of a criterion based on the maximum likelihood function rather than least squares minimization.

MGE MRI sequence

We used a MGE sequence for data collection due to its relatively short *TE*, permitting both the detection of rapidly-decaying signal components and good digitization of the transverse decay. We were motivated by the potential applicability of this sequence to measurement of component fractions and T_2^* values within cartilage. Our simulations and phantom measurements indicated that analysis of MGE data using M_R or M_G permits estimation of these parameters from magnitude MR images obtained under clinical conditions and with only moderate SNR.

Recent preliminary studies applied the UTE sequence to the problem of obtaining multi-component T_2^* data (21-25). However, UTE sequences remain specialized and are not available routinely. Further, current implementations of UTE do not permit acquisition of echo trains in a single shot, but rather require a separate acquisition for each *TE*. This leads to either longer acquisition times or to a limitation on the frequency or duration of decay sampling. Finally, the Cartesian sampling of the MGE sequence is often preferred over the radial sampling of the UTE sequence because the former is less prone to off-resonance effects. Nevertheless, the main purpose of this paper, to demonstrate the role of Rician noise in the analysis of biexponential data, is independent of the specific pulse sequence used.

It is well-known that T_2^* exhibits contributions from both microscopic magnetic field fluctuations leading to irreversible signal dephasing, characterized by T_2, and from fixed magnetic field gradients corresponding to mesoscopic or macroscopic field inhomogeneities, characterized by $T_2^{'}\sim 2\pi/\gamma\Delta B_0$ (49), where γ is the gyromagnetic ratio and ΔB_0 is the inhomogeneity of the magnetic field B_0. Given $1/T_{2,s}^*=1/T_{2,s}+1/T_2^{'}$ and $1/T_{2,l}^*=1/T_{2,l}+1/T_2^{'}$, $T_{2,s}^*$ is expected to be largely dominated by $T_{2,s}$, while $T_{2,l}^*$ is likely

more heavily influenced by T_2'. This complicates the interpretation of $T_{2,l}^*$ in terms of $T_{2,l}$. The complications arising from T_2' effects can be minimized through use of localized higher order shimming (50-51) and small voxels.

Simulations, phantom and ex-vivo studies

Simulations show that in the limit of high SNR, all four methods yielded accurate and precise results. At lower SNR, we found that although M_R shows the lowest fit errors, M_G provides comparable accuracy and precision in many cases. For example, the fraction of the rapidly decaying component F_s, and $T_{2,l}^*$ were estimated with accuracy and precision of at least 2% and 10%, respectively. Somewhat larger SNR (SNR > 60), still readily achievable clinically, was required to quantify $T_{2,s}^*$. In addition, the computation time using M_G was substantially lower than that required for M_R. This may be especially important for reconstruction of 3D parameter maps. These qualitative comparisons between methods were observed for both PCI and CI, and over a wide range of relaxation times and component fractions.

As seen from Tables 2 and 3, there is a more stringent SNR requirement for accurately and precisely characterizing the smaller, more rapidly relaxing, as compared to the slowly relaxing component. This is in contrast to the case for bone, in which the rapidly relaxing component is the larger one (52). Indeed, in the latter case, mapping of the smaller, slowly relaxing fraction, requires larger SNR than for the long component. In all cases, acquisition parameters such TE_1, ΔTE and the number of echoes directly affect bias and dispersion.

There was good overall agreement between our simulation results and phantom measurements. In particular, both M_G and M_R were found to be the most effective methods, especially in the setting of limited SNR. The bias and dispersion of all estimated parameters for a given SNR were lower in the simulations (Figs. 2 and 4, Tables 2 and 3). Several factors may account for this. First, the spatial variation of the B_1 and B_0 fields would be expected to produce local variation of SNR and T_2', respectively. In addition, the initial estimates for the nonlinear fits, $\hat{\theta}_{l,init}$, were known for the simulations while in the case of phantoms, incorrect initial estimates may have produced local, rather than global, minima in the least squares routine. It is important to emphasize that for the phantom and *ex-vivo* tissue studies, the reference measurements themselves are affected by noise, which then propagates into the final results.

All investigations showed sensitivity of all fitting methods to initial estimates. This highlighted the necessity for establishing a reproducible algorithm for selection of these estimates, especially in the low SNR regime. In contrast, at high SNR, convergence was attained even for relatively poor initial estimates. In all cases, we used the curve peeling algorithm described above to select the estimates.

Ex-vivo measurements showed nonexponential and monoexponential behavior in several voxels of the investigated samples. The nonexponential behavior, more pronounced at 7T, was restricted to the periphery of the samples and adjacent to blood vessels. This is consistent with the large susceptibility gradients in those regions (53). The same phenomena

were also observed by Qian (21-22) at 3T. Monoexponential behavior is attributable to several factors including the requisite SNR for detecting the short fraction and the sensitivity of the NNLS fit to noise. In addition, the possibility that the sample exhibits a single relaxation pool, or pools in rapid exchange, in those regions cannot be excluded. Finally, Fig 7 shows that M_R provides the most accurate and precise analysis, especially in the low-to-moderate SNR regime. At high SNR, our investigations indicate that any of the four methods evaluated here could be used to achieve high accuracy and precision.

The parameter maps in Fig 5 showed heterogeneity of voxel values. Given the voxel-by-voxel fit and the difficulty of the inversion in the presence of noise, there is the potential for numerical instability, resulting in apparently discontinuous voxel values. In addition, there is well-known micro-heterogeneity in the tissue itself. For high SNR ~135-145, there was minimal variation in the parametric maps (Fig. 3), consistent with the relatively homogeneous nature of the phantoms. Accordingly, the bulk of the heterogeneity seen in the BNC images in Fig 5, which were obtained at SNR ~140, were likely due to actual tissue micro-heterogeneities.

Our simulations, phantom and explant studies indicate that the SNR requirement for robust estimation of short and long T_2^* components is clinically achievable. Recent work (54) demonstrates the practicability of the SPGR sequence, which is similar to the MGE sequence, to map bicomponent T_2^* in human menisci. This study shows only few voxels exhibiting biexponential behavior using the M_T fitting method, possibly indicating the requirement for either a more sophisticated fitting approach or the need for increased SNR. Therefore, combining the MGE sequence for rapid data acquisition with the M_R method for data fitting may represent a promising approach to bicomponent mapping in human articular cartilage.

In the case of multiple receive coils, as implemented conventionally to increase speed and SNR, the signal model in the resulting magnitude images depends on the number of channels and other coil characteristics. If uncorrelated but equal noise amplitude among channels is assumed, the data distribution would be approximated by a generalized Rician distribution, that is, the non-central χ-distribution (29, 55).

Acknowledgments

We gratefully acknowledge the anonymous reviewers for their helpful comments. This work was supported by the Intramural Research Program of the NIH, National Institute on Aging.

Appendix

Explicit calculation of the first derivatives of $E_{Gauss}[S_M]$, $E_{Gauss}[S_M^2]$ and $E_{Rice}[S_M]$ with respect to each model parameter improves the speed and the robustness of the NLLS fits.

Gaussian noise distribution

The following first derivatives were provided to the NLLS fit of M_T and M_G and CRLB calculations as well.

$$\frac{\partial E_{Gauss}\left[S_M\right]}{\partial \theta_i}=\frac{\partial A\left(TE,\boldsymbol{\theta}\right)}{\partial \theta_i} \quad \text{[A. 1]}$$

so that

$$\begin{aligned}
\frac{\partial A\left(TE,\boldsymbol{\theta}\right)}{\partial PD}&=F_s\,exp\left(\frac{-TE}{T^*_{2,s}}\right)+\left(1-F_s\right)exp\left(-TE\Big/T^*_{2,l}\right)\\
\frac{\partial A\left(TE,\boldsymbol{\theta}\right)}{\partial F_s}&=PD\left(exp\left(-TE\Big/T^*_{2,s}\right)-exp\left(-TE\Big/T^*_{2,l}\right)\right)\\
\frac{\partial A\left(TE,\boldsymbol{\theta}\right)}{\partial T^*_{2,s}}&=F_s\,PD\frac{TE}{\left(T^*_{2,s}\right)^2}exp\left(-TE\Big/T^*_{2,s}\right)\\
\frac{\partial A\left(TE,\boldsymbol{\theta}\right)}{\partial T^*_{2,l}}&=PD\left(1-F_s\right)\frac{TE}{\left(T^*_{2,l}\right)^2}exp\left(-TE\Big/T^*_{2,l}\right)
\end{aligned} \quad \text{[A. 2]}$$

McGibney noise distribution

$$\frac{\partial E_{Gauss}\left[S^2_M\right]}{\partial \theta_i}=\frac{\partial A^2\left(TE,\boldsymbol{\theta}\right)}{\partial \theta_i} \quad \text{[A. 3]}$$

so that

$$\begin{aligned}
\frac{\partial A^2\left(TE,\boldsymbol{\theta}\right)}{\partial PD}&=2PD\left(F_s\,exp\left(-TE\Big/T^*_{2,s}\right)+\left(1-F_s\right)exp\left(-TE\Big/T^*_{2,l}\right)\right)^2\\
\frac{\partial A^2\left(TE,\boldsymbol{\theta}\right)}{\partial F_s}&=2PD^2\left(F_s\,exp\left(-2TE\Big/T^*_{2,s}\right)+\left(F_s-1\right)exp\left(-2TE\Big/T^*_{2,l}\right)\right.\\
&\quad\left.+\left(1-2F_s\right)exp\left(-TE\left(1\Big/T^*_{2,s}+1\Big/T^*_{2,l}\right)\right)\right)\\
\frac{\partial A^2\left(TE,\boldsymbol{\theta}\right)}{\partial T^*_{2,s}}&=\frac{2F_s\;TE\;PD^2}{\left(T^*_{2,s}\right)^2}\left(F_s\,exp\left(-2TE\Big/T^*_{2,s}\right)+\left(1-F_s\right)exp\left(-TE\left(1\Big/T^*_{2,s}+1\Big/T^*_{2,l}\right)\right)\right)\\
\frac{\partial A^2\left(TE,\boldsymbol{\theta}\right)}{T^*_{2,l}}&=\frac{2\left(1-F_s\right)TE\;PD^2}{\left(T^*_{2,l}\right)^2}\left(\left(1-F_s\right)exp\left(-2TE\Big/T^*_{2,l}\right)+F_s\,exp\left(-TE\left(1\Big/T^*_{2,s}+1\Big/T^*_{2,l}\right)\right)\right)
\end{aligned} \quad \text{[A. 4]}$$

Rician noise distribution

The derivative of the modified n[th] order Bessel function is given by (56)

$$\frac{\partial I_n\left(\alpha\right)}{\partial \alpha}=I_{n-1}\left(\alpha\right)-\frac{n}{\alpha}I_n\left(\alpha\right)=\frac{n}{\alpha}I_n\left(\alpha\right)+I_{n+1}\left(\alpha\right) \quad \text{[A. 5]}$$

Using Eq. 2 and Eq. A.5,

$$\frac{\partial E_{Rice}[S_M]}{\partial \theta_i} = \frac{\partial E_{Rice}[S_M]}{\partial \alpha} \frac{\partial \alpha}{\partial A(TE,\boldsymbol{\theta})} \frac{\partial A(TE,\boldsymbol{\theta})}{\partial \theta_i} \quad [A6]$$

with

$$\begin{aligned} \frac{\partial E_{Rice}[S_M]}{\partial \alpha} \frac{\partial \alpha}{\partial A(TE,\boldsymbol{\theta})} &= \sigma \sqrt{\tfrac{\pi}{2}} e^{-\alpha} (I_0(\alpha) + I_1(\alpha)) \frac{A(TE,\boldsymbol{\theta})}{2\sigma^2} \\ &= \sqrt{\alpha \tfrac{\pi}{2}} e^{-\alpha} (I_0(\alpha) + I_1(\alpha)) \end{aligned} \quad [A. 7]$$

where $\alpha = (A(TE, \theta)/2\sigma)^2$. $\partial A(TE, \theta)/\partial \theta_i$ was calculated for each estimated parameter, θ_i, according to Eq. A.1.

References

1. Mosher TJ, Dardzinski BJ. Cartilage MRI T2 relaxation time mapping: overview and applications. Semin Musculoskelet Radiol. 2004; 8:355–368. [PubMed: 15643574]
2. Lattanzio PJ, Marshall KW, Damyanovich AZ, Peemoeller H. Macromolecule and Water Magnetization Exchange Modeling in Articular Cartilage. Magn Reson Med. 2000; 44:840–851. [PubMed: 11108620]
3. Ghiassi-Nejad M, Torzilli PA, Peemoeller H, Pintar MM. Proton spin-spin relaxation study of molecular dynamics and proteoglycan hydration in articular cartilage. Biomaterials. 2000; 21:2089–2095. [PubMed: 10966019]
4. Lattanzio PJ, Marshall KW, Damyanovich AZ, Peemoeller H. Characterization of Proteoglycan Depletion in Articular Cartilage using Two-Dimensional Time Domain Nuclear Magnetic Resonance. Magn Reson Med. 2005; 54:1397–1402. [PubMed: 16265632]
5. Shinar H, Navon G. Multinuclear NMR and microscopic MRI studies of the articular cartilage nanostructure. NMR Biomed. 2006; 19:877–893. [PubMed: 17075957]
6. Keinan-Adamsky K, Shinar H, Navon G. Multinuclear NMR and MRI studies of the Maturation of Pig Articular Cartilage. Magn Reson Med. 2006; 55:532–540. [PubMed: 16450338]
7. Reiter DA, Roque RA, Lin PC, Doty SB, Pleshko N, Spencer RG. Improved specificity of cartilage matrix evaluation using multiexponential transverse relaxation analysis applied to pathomimetically degraded cartilage. NMR Biomed. 2011; 24:1286–1294. [PubMed: 21465593]
8. Reiter DA, Irrechukwu R, Lin PC, Moghadam S, Thaer SV, Pleshko N, Spencer RG. Improved MR-based characterization of engineered cartilage using multiexponential T_2 relaxation and multivariate analysis. NMR Biomed. 2012; 25:476–488. [PubMed: 22287335]
9. Reiter DA, Lin PC, Fishbein KW, Spencer RG. Multicomponent T_2 relaxation analysis in cartilage. Magn Reson Med. 2009; 61:803–809. [PubMed: 19189393]
10. Reiter DA, Roque RA, Lin PC, Irrechukwu O, Doty S, Longo DL, Pleshko N, Spencer RG. Mapping Proteoglycan-Bound Water in Cartilage: Improved Specificity of Matrix Assessment Using Multiexponential Transverse Relaxation Analysis. Magn Reson Med. 2011; 65:377–384. [PubMed: 21264931]
11. Rice, SO. Mathematical analysis of random noise. In: Wax, N., editor. Selected papers on noise and stochastic processes. New York, NY: Dover Publications Inc.; 1954. p. 133-194.
12. Bernstein MA, Thomasson DM, Perman WH. Improved detectability in low signal-to-noise ratio magnetic resonance images by means of phase-corrected real reconstruction. Med Phys. 1989; 16:813–817. [PubMed: 2811764]
13. Raya JG, Dietrich O, Horng A, Weber J, Reiser MF, Glaser C. T_2 Measurement in Articular Cartilage: Impact of the Fitting Method on Accuracy and Precision at Low SNR. Magn Reson Med. 2010; 63:181–193. [PubMed: 19859960]

14. Karlsen OT, Verhagen R, Bovée WMMJ. Parameter Estimation From Rician-Distributed Data Sets Using a Maximum Likelihood Estimator: Application to T_1 and Perfusion Measurements. Magn Reson Med. 1999; 41:614–623. [PubMed: 10204887]
15. Dietrich O, Raya JG, Reiser MF. Magnetic Resonance Noise Measurements and Signal Quantization Effects at Very Low Noise Levels. Magn Reson Med. 2008; 60:1477–1487. [PubMed: 19025912]
16. Gudbjartsson H, Patz S. The Rician Distribution of Noisy MRI Data. Magn Reson Med. 1995; 34:910–914. [PubMed: 8598820]
17. Kristoffersen A. Estimating Non-Gaussian Diffusion Model Parameters in the Presence of Physiological Noise and Rician Signal Bias. J Magn Reson Imaging. 2012; 35:181–189. [PubMed: 21972173]
18. McGibney G, Smith MR. An unbiased signal-to-noise ratio measure for magnetic resonance imaging. Med Phys. 1993; 20:1077–1078. [PubMed: 8413015]
19. Carr HY, Purcell EM. Effects of Diffusion on Free Precession in Nuclear Magnetic Resonance Experiments. Phys Rev. 1954; 94:630–637.
20. Meiboom S, Gill D. Modified spin-echo method for measuring nuclear relaxation times. Rev Sci Intrum. 1958; 29:688–691.
21. Qian Y, Williams AA, Chu CR, Boada FE. Multicomponent T_2* Mapping of Knee Cartilage: Technical Feasibility *ex-vivo*. Magn Reson Med. 2010; 64:14–1432.
22. Qian Y, Williams AA, Chu CR, Boada FE. Repeatability of Ultrashort Echo Time-Based Two-Component T_2* Measurements on Cartilages in Human Knee at 3T. Magn Reson Med. 2013; 69:1565–1572.
23. Pauli C, Bae WC, Lee M, Lotz M, Bydder GM, D'Lima DL, Chung CB, Du J. Ultrashort-Echo Time MR Imaging of the Patella with Bicomponent Analysis: Correlation with Histopathologic and Polarized Light Microscopic Findings. Radiology. 2012; 264:484–493. [PubMed: 22653187]
24. Du J, Diaz E, Carl M, Bae W, Chung CB, Bydder GM. Ultrashort Echo Time Imaging With Bicomponent Analysis. Magn Reson Med. 2012; 67:645–649. [PubMed: 22034242]
25. Diaz E, Chung CB, Bae WC, Statum S, Znamirowski R, Bydder GM, Du J. Ultrashort echo time spectroscopic imaging (UTESI): an efficient method for quantifying bound and free water. NMR Biomed. 2012; 25:161–168. [PubMed: 21766381]
26. Papoulis, A. Probability, random variables and stochastic processes. 2. McGraw-Hill; Tokyo: 1984.
27. Sijbers J, den Dekker AJ, Verhoye M, Van Audekerke J, Van Dyck D. Estimation of noise from magnitude MR images. Magn Reson Imag. 1998; 16:87–90.
28. Edelstein WA, Bottomley PA, Pfeifer LM. A signal-to-noise calibration procedure for NMR imaging systems. Med Phys. 1984; 11:180–185. [PubMed: 6727793]
29. Constantinides CD, Atalar E, McVeigh ER. Signal-to-Noise Measurements in Magnitude Images from NMR Phased Arrays. Magn Reson Med. 1997; 38:852–857. [PubMed: 9358462]
30. Sijbers J, den Dekker AJ. Maximum Likelihood Estimation of Signal Amplitude and Noise Variance From MR Data. Magn Reson Med. 2004; 51:586–594. [PubMed: 15004801]
31. Jones JA, Hodgkinson P, Barker AL, Hore PJ. Optimal sampling strategies for the measurement of spin-spin relaxation times. J Magn Reson. 1996; 113:25–34.
32. Zhang Y, Yeung HN, O'Donnell O, Carson PL. Determination of Sample Time for T_1. J Magn Reson Imaging. 1998; 8:675–681. [PubMed: 9626885]
33. Anastasiou A, Hall LD. Optimization of T_2 and M_0 measurements of biexponential systems. Magn Reson Imaging. 2004; 22:67–80. [PubMed: 14972396]
34. Bonny JM, Zanca M, Boire JY, Veyre A. T_2 maximum likelihood estimation from multiple spin echo magnitude images. Magn Reson Med. 1996; 36:287–293. [PubMed: 8843383]
35. Alexander DC. A general framework for experiment design in diffusion MRI and its application in measuring direct tissue-microstructure features. Magn Reson Med. 2008; 60:439–448. [PubMed: 18666109]

36. Caan MWA, Khedoe HG, Poot DHJ, den Dekker AJ, Olabarriaga SD, Grimbergen KA, van Vliet LJ, Vos FM. Estimation of Diffusion Properties in Crossing Fiber Bundles. IEEE Trans Med Imaging. 2010; 29:1504–1515. [PubMed: 20562045]
37. Cramer, H. Mathematical Methods of Statistics. Princeton University Press; Princeton: 1946.
38. Poot DHJ, den Dekker AJ, Achten E, Verhoye M, Sijbers J. Optimal Experimental Design for Diffusion Kurtosis Imaging. IEEE Trans Med Imaging. 2010; 29:819–829. [PubMed: 20199917]
39. Miller AJ, Joseph PM. The use of power images to perform quantitative analysis on low SNR MR Images. Magn Reson Imaging. 1993; 11:1051–1056. [PubMed: 8231670]
40. Levene, H. Robust tests for equality of variances. In: Olkin, I.; Ghurge, SG.; Höeffding, A.; Madow, WG.; Mann, HB., editors. Contributions to probability and statistics: essays in honor of Harold Hotelling. Stanford, CA: Stanford University Press; 1960. p. 288-292.
41. Marquardt D. An algorithm for least squares estimation of nonlinear parameters. SIAM J Appl Math. 1963; 11:431–441.
42. Hoaglin, D.; Mosteller, F.; Tukey, J. Understanding Robust and Exploratory Data Analysis. New York: John Wiley & Sons; 1983.
43. Bonny JM, Laurent W, Renou JP. Detection of susceptibility effects using simultaneous T_2* and magnetic field mapping. Magn Reson Imaging. 2000; 18:1125–1128. [PubMed: 11118767]
44. Reeder, SB.; Vu, AT.; Hargreaves, BA.; Shimakawa, A.; Wieben, O.; McKenzie, CA.; Polzin, JA.; Brittain, JH. Rapid 3D-SPGR imaging of the liver with Multi-echo IDEAL. Proceedings of the ISMRM; Seattle, WA. 2006.
45. Hutton C, Bork A, Josephs O, Deichmann R, Ashburner J, Turner R. Image Distortion Correction in fMRI: A Quantitative Evaluation. NeuroImage. 2002; 16:217–240. [PubMed: 11969330]
46. Woods RP, Grafton ST, Holmes CJ, Cherry SR, Mazziotta JC. Automated image registration: I. General methods and intrasubjectintramodality validation. J Comput Assist Tomogr. 1998; 22:139–152. [PubMed: 9448779]
47. Woods RP, Grafton ST, Watson JDG, Sicotte NL, Mazziotta JC. Automated image registration: II. Intersubject validation of linear and nonlinear models. J Comput Assist Tomogr. 1998; 22:153–165. [PubMed: 9448780]
48. Motulsky, H.; Christopoulos, A. Fitting Models to Biological Data using Linear and Nonlinear Regression. New York: Oxford University Press; 2004.
49. Yablonskiy DA. Quantitation of intrinsic magnetic susceptibilityrelated effects in a tissue matrix. Phantom study. Magn Reson Med. 1998; 39:417–428. [PubMed: 9498598]
50. Kim DH, Adalsteinsson E, Glover GH, Spielman DM. Regularized Higher-Order *In-vivo* Shimming. Magn Reson Med. 2002; 48:715–722. [PubMed: 12353290]
51. Hetherington HP, Kuznetsov AM, Avdievich NI, Pan JW. Higher Order B_0 Shimming of the Human Brain at 7T. Proc Intl Soc Mag Reson Med. 2009; 17
52. Du J, Bydder GM. Qualitative and quantitative ultrashort-TE MRI of cortical bone. NMR Biomed. 2013; 26:489–506. [PubMed: 23280581]
53. Yablonskiy DA, Haacke EM. Theory of NMR signal behavior in magnetically inhomogeneous tissues: The static dephasing regime. Magn Reson Med. 1994; 32:749–763. [PubMed: 7869897]
54. Juras V, Apprich S, Zbýň S, Zak L, Deligianni X, Szomolanyi P, Bieri O, Trattnig S. Quantitative MRI analysis of menisci using biexponential T_2* fitting with a variable echo time sequence. Magn Reson Med. 201310.1002/mrm.24760
55. Miller, KS. Multidimensional Gaussian Distributions. New York: John Wiley and Sons; 1964.
56. Abramowitz, M.; Stegun, IA. Handbook of mathematical functions. New York: Dover Publications, Inc; 1965.

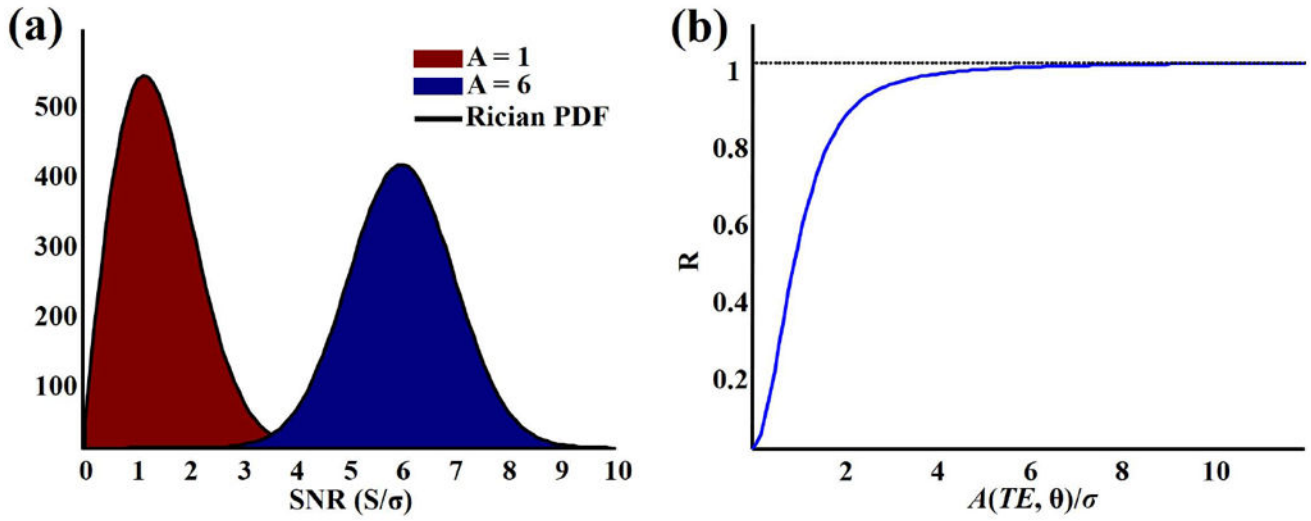

Fig. 1.

(a) Histograms of Rician simulated data, given by Eq. 13, for two signal amplitudes (A = 1 and 6, σ = 1) and their corresponding Rician PDF given by Eq. 1. The Rician distribution approaches a Gaussian when SNR ≥ 6. (b) The factor R as a function of SNR given by Eq. 8. R represents the correction factor for the Fisher matrix for Rician data. R approaches 1 when SNR ≥ 6.

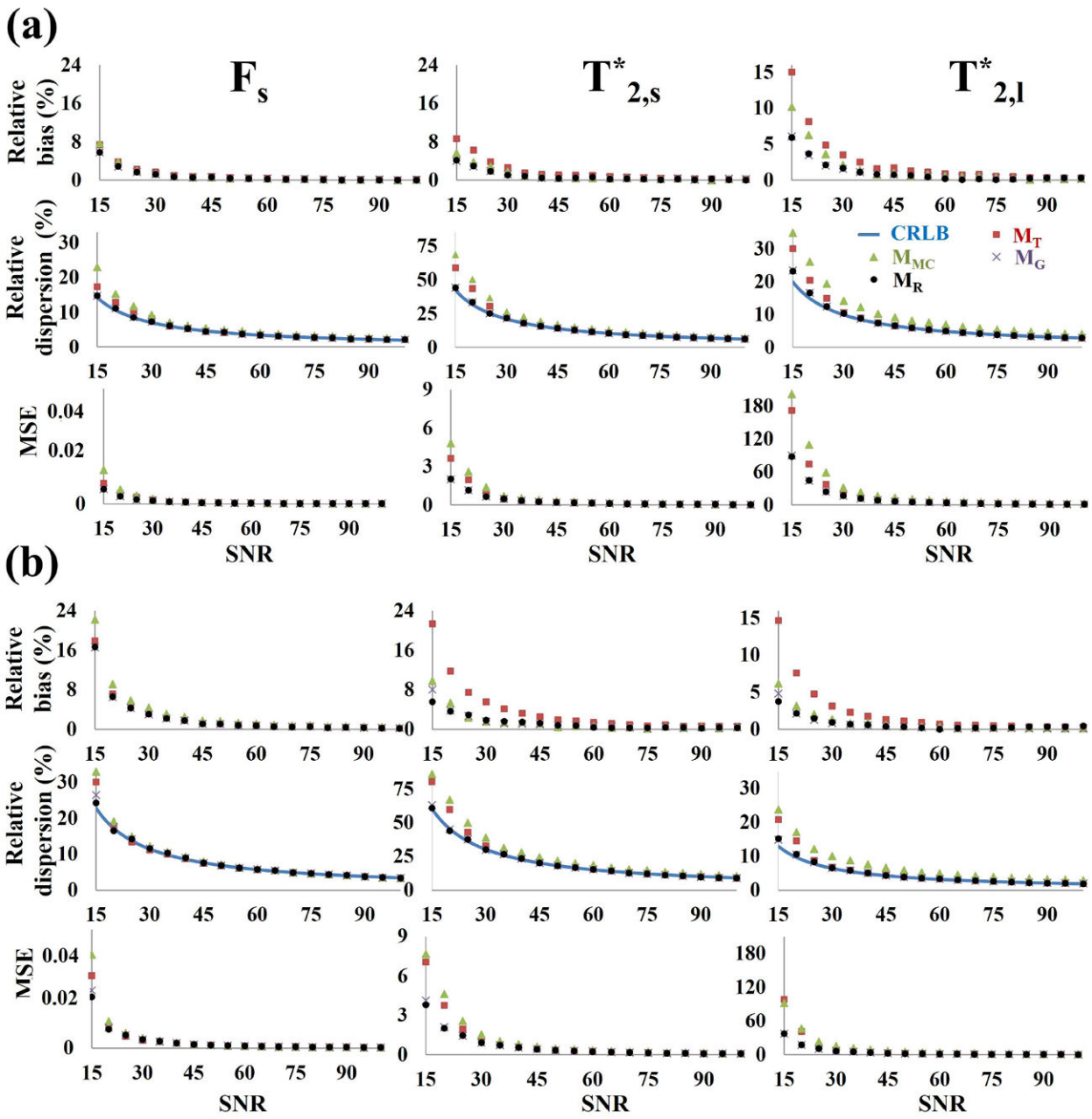

Fig. 2.

Simulation results showing relative bias (uppermost row), relative dispersion (middle row) and mean-squared-error (lowermost row) for F_s, $T^*_{2,s}$ and $T^*_{2,l}$ as a function of SNR using the fitting methods M_T, M_{Mc}, M_G and M_R for (a) PCI and (b) CI acquisition conditions.

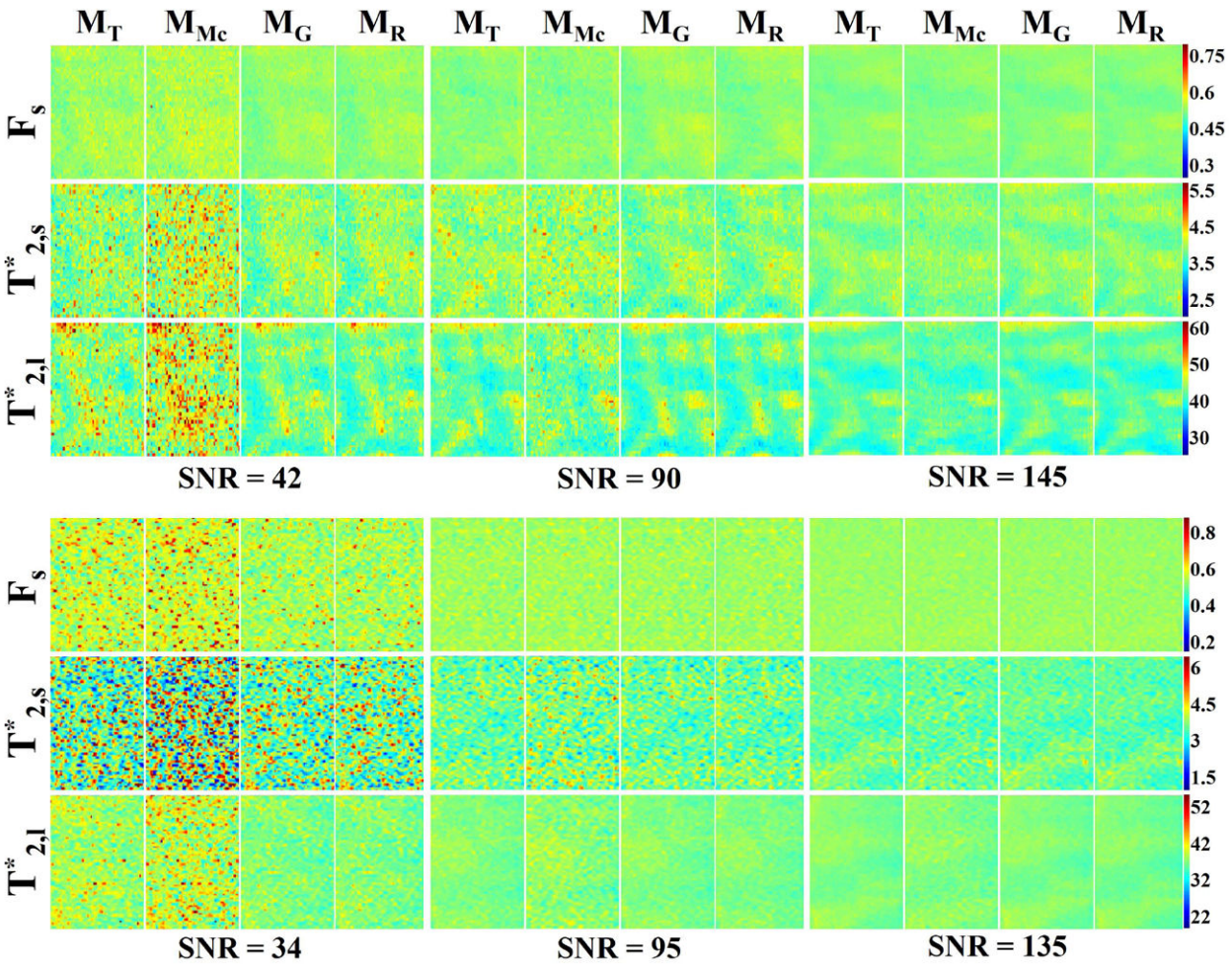

Fig. 3.

Representative F_s, $T^*_{2,s}$ and $T^*_{2,l}$ maps from the two-component doped water phantom obtained using the fitting methods M_T, M_{Mc}, M_G and M_R at 7T (upper panel) for SNR = 42, 90, 145 and at 3T (lower panel) for SNR = 34, 95, 135.

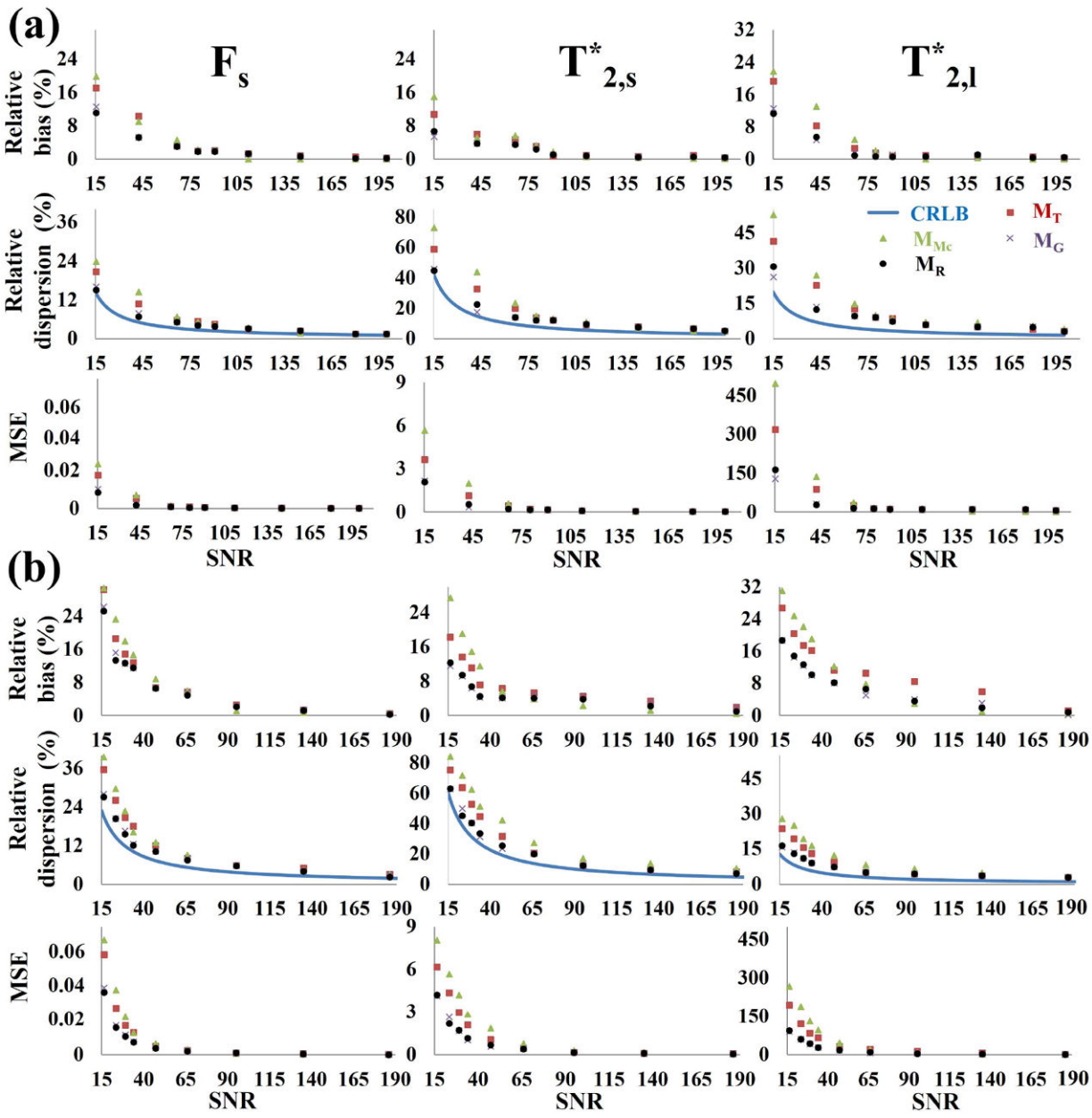

Fig. 4.

Phantom imaging results showing relative bias (uppermost row), relative dispersion (middle row) and mean-squared-error (lowermost row) of F_s, $T^*_{2,s}$ and $T^*_{2,l}$ as a function of SNR using M_T, M_{Mc}, M_G and M_R obtained at (a) 7T and (b) 3T.

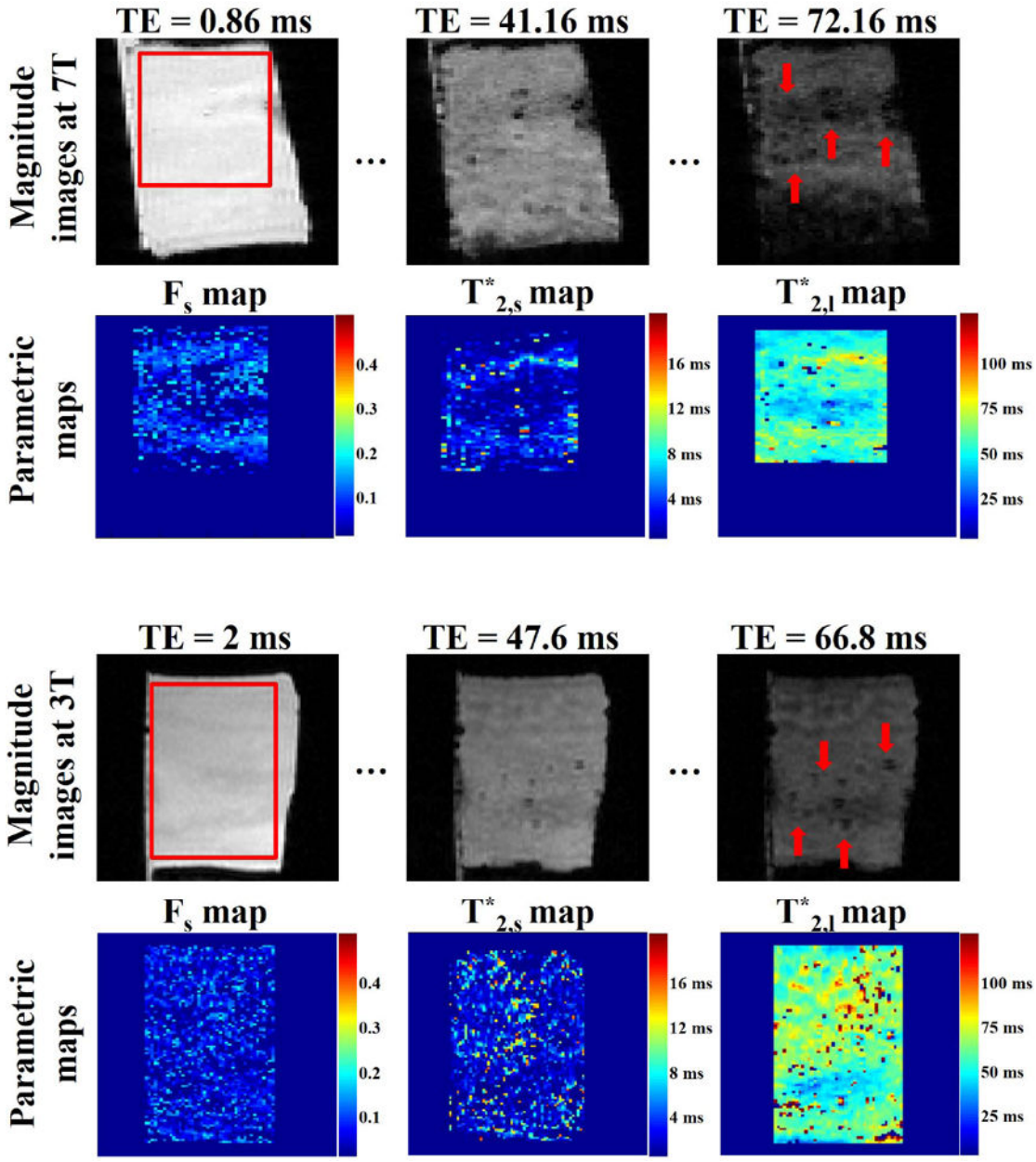

Fig. 5.

Magnitude MR images of BNC obtained at the indicated echo times at 7T (top two rows) and 3T (bottom two rows). Red squares indicate the region of the samples where the parametric maps of F_s, $T^*_{2,s}$ and $T^*_{2,l}$ were obtained. The parametric maps presented here were obtained at high SNR using the Rician method, M_R. Red arrows indicates region of blood vessels.

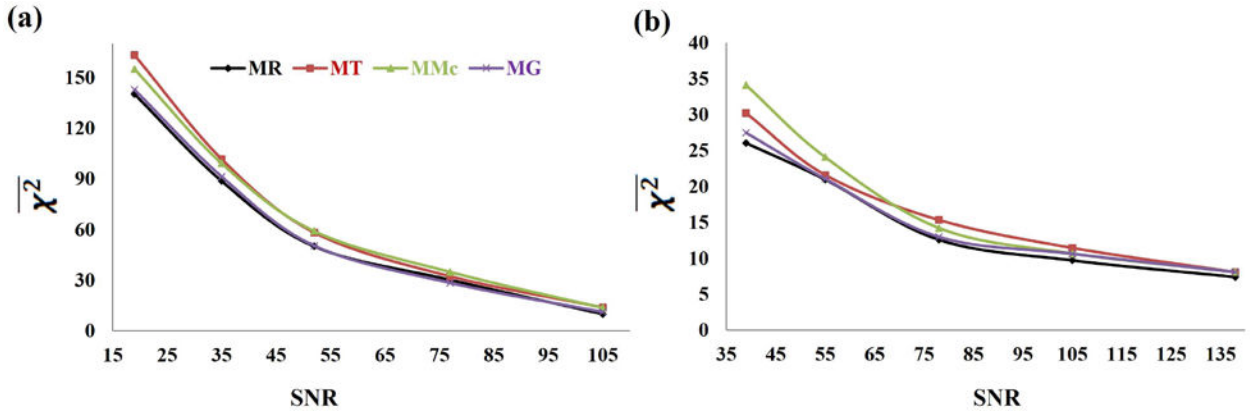

Fig. 6.

Mean chi-square, $\overline{\chi^2}$, for biexponential fitting of BNC images using M_T, M_{Mc}, M_G and M_R as a function of SNR at a) 7T and b) 3T.

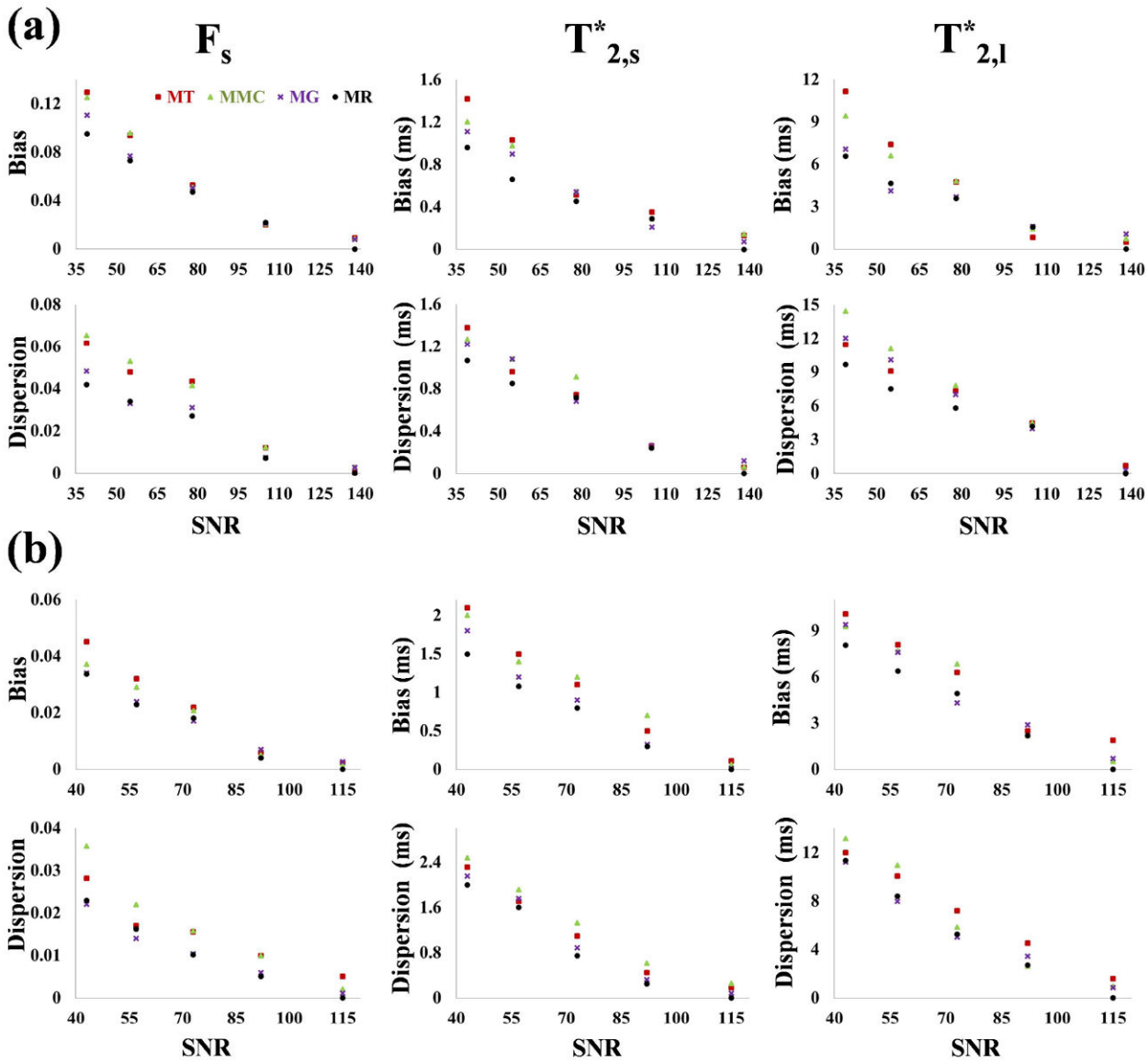

Fig. 7.

Ex-vivo BNC imaging results showing absolute bias (upper row) and absolute dispersion (lower row) for F_s, $T^*_{2,s}$ and $T^*_{2,l}$ as a function of SNR using M_T, M_{Mc}, M_G and M_R (a) for PCI acquisition conditions at 7T and (b) for CI acquisition conditions at 3T. Parametric maps obtained with M_R at high SNR were considered to be reference maps. The values of the voxels exhibiting monoexponential or nonexponential behavior were set to zero.

Table 1

Values of the mean (over $15 \leq SNR \leq 40$) and the maximum (at SNR = 15) number of voxels with extreme outliers, VEO, removed for each fitting method (M_T, M_{Mc}, M_G and M_R; see "Methods comparison" section) from Monte Carlo simulations using input parameters for both PCI and CI conditions. VEO values expressed as a percent of the total 4900 voxels evaluated.

	M_T		M_{Mc}		M_G		M_R	
*VEO (%) / Condition	$15 \leq SNR \leq 40$	SNR = 15	$15 \leq SNR \leq 40$	SNR = 15	$15 \leq SNR \leq 40$	SNR = 15	$15 \leq SNR \leq 40$	SNR = 15
PCI	2.9	11	3.3	12.1	2.2	11.8	2.1	11.6
CI	5.7	17.1	6.5	16	5.8	14.9	5.5	15.8

*VEO: number of voxels with extreme outliers.

Table 2

Relative accuracy and precision obtained by Monte Carlo simulations for the estimation of F_s, $T^*_{2,s}$ and $T^*_{2,l}$ at SNR = 15 and 100 using the M_T, M_{Mc}, M_G and M_R methods for five different combination of input parameters F_s, $T^*_{2,s}$ and $T^*_{2,l}$. $\hat{F_s}$, $\hat{T}^*_{2,s}$ and $\hat{T}^*_{2,l}$ represent the derived parameter estimates.

	M_T				M_{Mc}				M_G				M_R			
	Accuracy (%)		Precision (%)		Accuracy (%)		Precision (%)		Accuracy (%)		Precision (%)		Accuracy (%)		Precision (%)	
SNR	15	100	15	100	15	100	15	100	15	100	15	100	15	100	15	100
$F_s = 0.3, T^*_{2,s}=4\ ms$ and $T^*_{2,l}=40\ ms$																
$\hat{F_s}$	44	2	58	5	56	2	71	5	38	1	50	5	37	1	51	5
$\hat{T}^*_{2,s}$	24	1	80	15	18	1	93	15	17	0	74	13	14	0	74	14
$\hat{T}^*_{2,l}$	14	1	20	2	11	1	23	2	5	0	16	2	5	0	15	3
$F_s = 0.5, T^*_{2,s}=4\ ms$ and $T^*_{2,l}=40\ ms$																
$\hat{F_s}$	14	0	32	3	18	0	34	4	6	0	22	3	5	0	21	3
$\hat{T}^*_{2,s}$	16	0	71	8	10	0	78	9	4	0	59	8	2	0	63	8
$\hat{T}^*_{2,l}$	21	0	21	3	9	0	24	3	6	0	19	2	3	0	17	3
$F_s = 0.7, T^*_{2,s}=4\ ms$ and $T^*_{2,l}=40\ ms$																
$\hat{F_s}$	5	0	6	1	6	0	13	1	3	0	7	2	2	0	7	2
$\hat{T}^*_{2,s}$	8	0	35	4	9	0	44	5	3	0	30	5	1	0	28	5
$\hat{T}^*_{2,l}$	35	1	42	4	15	1	58	4	12	0	31	4	8	0	31	4
$F_s = 0.3, T^*_{2,s}=4\ ms$ and $T^*_{2,l}=20 ms$																
$\hat{F_s}$	81	7	74	8	78	9	81	14	69	2	68	9	58	1	61	8

	M_T				M_{Mc}				M_G				M_R			
	Accuracy (%)		Precision (%)		Accuracy (%)		Precision (%)		Accuracy (%)		Precision (%)		Accuracy (%)		Precision (%)	
SNR	15	100	15	100	15	100	15	100	15	100	15	100	15	100	15	100
$\hat{T}^*_{2,s}$	47	10	98	19	12	7	114	29	18	2	91	18	6	2	89	18
$\hat{T}^*_{2,l}$	57	3	92	5	10	2	31	7	22	0	38	4	8	0	23	3
$F_s = 0.3$, $T^*_{2,s}=4\ ms$ and $T^*_{2,l}=12\ ms$																
$\hat{F}_s$	205	50	273	49	90	39	197	56	121	20	208	37	68	6	187	30
$\hat{T}^*_{2,s}$	97	31	302	36	27	12	320	48	101	3	223	32	14	1	244	29
$\hat{T}^*_{2,l}$	585	13	93	17	22	8	61	21	9	4	57	9	20	1	42	7

Table 3

Relative accuracy and precision obtained for phantom measurements at 3T for the estimation of F_s, $T^*_{2,s}$ and $T^*_{2,l}$ at three different SNR levels using the M_T, M_{Mc}, M_G and M_R methods for three different values of F_s. $\hat{F_s}$, $\hat{T}^*_{2,s}$ and $\hat{T}^*_{2,l}$ represent the derived parameter estimates.

	M_T						M_{Mc}						M_G						M_R					
	Accuracy (%)			Precision (%)			Accuracy (%)			Precision (%)			Accuracy (%)			Precision (%)			Accuracy (%)			Precision (%)		
F_s = 0.3, $T^*_{2,s}$=3.3 ms and $T^*_{2,l}$=38.1 ms																								
SNR	18	53	105	18	53	105	18	53	105	18	53	105	18	53	105	18	53	105	18	53	105	18	53	105
$\hat{F_s}$	69	22	10	83	22	10	81	15	11	94	26	10	63	14	9	79	20	9	58	13	7	76	18	9
$\hat{T}^*_{2,s}$	25	8	1	121	39	18	29	9	1	114	45	21	14	4	3	98	35	18	13	2	0	98	32	18
$\hat{T}^*_{2,l}$	16	2	0	14	6	3	11	1	0	19	7	4	9	1	0	12	6	4	8	0	0	12	5	3
F_s = 0.5, $T^*_{2,s}$=3.3 ms and $T^*_{2,l}$=38.1 ms																								
SNR	16	47	94	16	47	94	16	47	94	16	47	94	16	47	94	16	47	94	16	47	94	16	47	94
$\hat{F_s}$	30	7	3	36	12	6	31	9	1	39	13	6	26	6	2	28	10	6	25	6	2	27	10	5
$\hat{T}^*_{2,s}$	18	6	5	75	32	12	27	6	2	84	42	17	11	4	4	63	23	12	12	4	3	63	25	12
$\hat{T}^*_{2,l}$	27	11	9	24	9	3	31	12	3	28	12	5	18	8	4	16	7	3	18	8	3	16	7	3
F_s = 0.7, $T^*_{2,s}$=3.3 ms and $T^*_{2,l}$=38.1 ms																								
SNR	13	41	86	13	41	86	13	41	86	13	41	86	13	41	86	13	41	86	13	41	86	13	41	86
$\hat{F_s}$	5	4	3	12	4	2	6	4	3	14	5	2	4	3	2	11	3	1	4	3	2	10	3	1
$\hat{T}^*_{2,s}$	8	5	4	43	13	7	9	6	5	49	17	10	8	3	3	38	12	6	7	3	3	36	11	6
$\hat{T}^*_{2,l}$	60	17	8	30	8	5	45	15	9	33	12	6	41	13	7	23	6	4	37	13	7	24	6	4